

# Rotation Effect on Jet Impingement Heat Transfer in Smooth Rectangular Channels with Film Coolant Extraction

JAMES A. PARSONS<sup>†</sup> and JE-CHIN HAN\*

*Turbine Heat Transfer Laboratory, Department of Mechanical Engineering,  
Texas A&M University, College Station, TX 77843-3123, USA*

*(Received in final form 17 August 1999)*

**The effect of channel rotation on jet impingement cooling by arrays of circular jets in twin channels was studied. Impinging jet flows were in the direction of rotation in one channel and opposite to the direction of rotation in the other channel. The jets impinged normally on the smooth, heated target wall in each channel. The spent air exited the channels through extraction holes in each target wall, which eliminates cross flow on other jets. Jet rotation numbers and jet Reynolds numbers varied from 0.0 to 0.0028 and 5000 to 10,000, respectively. For the target walls with jet flow in the direction of rotation (or opposite to the direction of rotation), as rotation number increases heat transfer decreases up to 25% (or 15%) as compared to corresponding results for non-rotating conditions. This is due to the changes in flow distribution and rotation induced Coriolis and centrifugal forces.**

*Keywords:* Gas turbine, Impingement cooling, Rotation heat transfer

## INTRODUCTION

Several methods such as film cooling, augmented cooling in internal serpentine channels and impingement cooling on internal surfaces are in use to cool turbine blades. Durability goals require these cooling methods for rotor blades of advanced gas turbine engines. Since any amount of coolant (air extracted from the compressor) penalizes engine performance, it is necessary to understand and to

optimize turbine cooling method employed, and the turbine blade geometry. Cooling rotor blades is complicated because rotation alters the motions of the blade internal coolant flow and hot external mainstream flow. Thus turbine blade heat transfer characteristics under rotating conditions are different from those for non-rotation.

The goal of this investigation is to extend the understanding of internal jet impingement cooling in channels for film-cooled turbine blades under

\* Corresponding author. Tel.: (409)845-3738. Fax: (409)862-2418. E-mail: jchan@mengr.tamu.edu.

<sup>†</sup> Present address: Combustion Turbine Engineering Department, Westinghouse Electric Corp., Orlando, FL 32826-2399, USA.

rotating conditions. Figure 1 shows cross sections of the test model. Jets in one array flow in the direction of rotation and impinge on the leading channel target wall, and jets in the other array flow opposite to the direction of rotation and impinge on the trailing channel target wall. The leading channel

flow (i.e., spent air) then passes through extraction holes in the target wall (extraction flow also in the direction of rotation) and exits the test model. The trailing channel flow passes through other extraction holes (this extraction flow is opposite to the direction of rotation) and exits the test model.

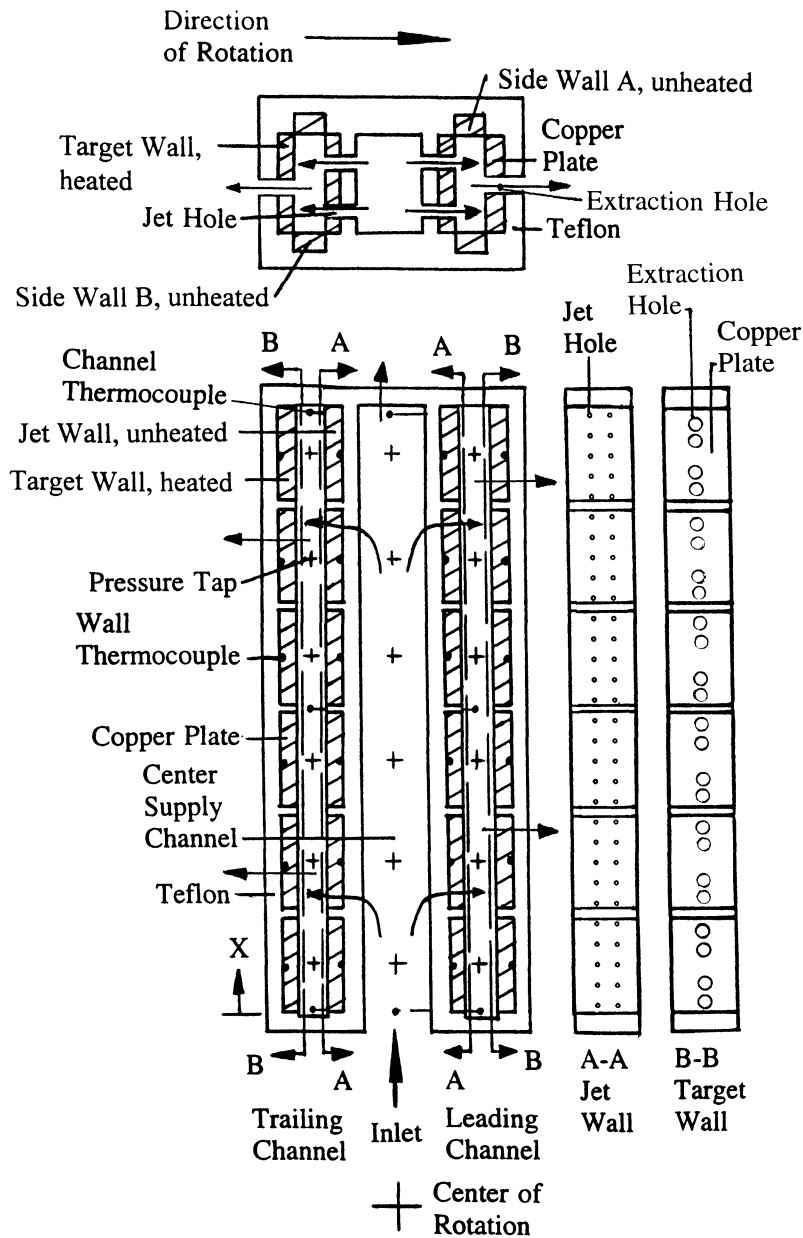


FIGURE 1 Test model schematic.

The spent air exited through the channels through extraction holes in each target wall, which eliminates cross flow effect on other jets, is to simulate an impingement-cooled rotating blade with film cooling conditions.

While investigations for impingement heat transfer by jet arrays with cross flow effect are numerous (Kercher and Tabakoff, 1970; Chance, 1974; Florschuetz *et al.*, 1981; Van Treuren *et al.*, 1994; Huang *et al.*, 1998), there are relatively few investigations for jet impingement heat transfer with film coolant extraction (also called impingement/effusion cooling, impingement/film cooling, and impingement with removal through vent holes). Hollworth and Dagan (1980), and Hollworth *et al.* (1983) varied jet Reynolds number and jet-to-jet spacing of square arrays on jet walls containing the effusion holes and found that staggered jet arrays with respect to effusion hole arrays on target walls out perform inline configurations for non-rotating target wall heat transfer. Andrews *et al.* (1988) studied non-rotating impingement and effusion cooling individually and in combination. While impingement and effusion cooling augment each other, the heat transfer coefficients for both effects simultaneously were lower than their sum. Al Dabagh *et al.* (1990) studied the effects of extraction number ratio ( $N_c/N_j$ ), extraction area ratio ( $A_c/A_j = D_c^2/D_j^2$ ), and jet-to-target wall distance on target wall and jet wall heat transfer in non-rotating rectangular channels. They found that the vortical flow (flow away from the heated target wall after impingement) which has gained heat at the target wall transfers its heat to the jet wall. The heat transfer coefficients for the jet wall may be up to 50% of those for the target wall. Bunker and Metzger (1990), and Metzger and Bunker (1990) used the transient liquid crystal technique to find that inline jet and extraction holes performed better than staggered hole for non-rotating, large scale model tests for the interior of a turbine blade leading edge.

Very few studies reported the effects of rotation on impingement cooling. Epstein *et al.* (1985) obtained heat transfer coefficients from a single

row of circular jets with radially outward cross flow in the leading edge region of a rotating blade. They concluded that rotation decreases the Nusselt number values up to 30% as compared to non-rotating results. Mattern and Hennecke (1996) presented local mass transfer data by using a naphthalene sublimation technique for a single row of circular jets with radially outward cross flow in the leading edge region of a rotating blade. They showed that rotation reduces the heat/mass transfer coefficients between 10% and 40% depending on the rotating angle. Similarly, Parsons and Han (1998) reported heat transfer behaviors in twin channels from an inline array of circular jets to simulate the mid-chord region of an impingement-cooled rotating blade. For that configuration, after the jets impinged on the target wall the flow turned and then exited the leading and trailing channels in the channel-wise (radially outward) direction. Thus flow from jets at smaller radii created a cross flow in the channel direction to jets at larger radii. They observed that regionally averaged heat transfer coefficients decrease up to 15% for jet flow in the direction of rotation and decrease up to 20% for jet flow opposite to the direction of rotation. Furthermore, Parsons *et al.* (1998) heated all four channel walls with cross flow and rotation, and found that the target wall and jet wall heat transfer coefficients decrease up to 20% with respect to those without rotation.

Instead of the cross flow exit configuration, this investigation will study film extraction through heated target walls. The film extraction holes minimize the degrading effects on impingement heat transfer due to cross flow. Specifically, the goal is to measure pressure to determine jet flow distributions and to measure temperatures to get regional surface convective heat transfer coefficients on smooth target walls in rectangular cross sectioned, orthogonally rotating, and twin channels with impingement cooling by an inline array of circular jets. The spent air exits each twin channel through a single row of extraction holes in the two target walls; the impinging jet and the extraction hole arrays are staggered. Non-rotating data will be taken to form

a baseline and to compare with previous non-rotating investigations. In addition, the effect of reducing the number of extraction holes by 50% will also be investigated.

### TEST STAND AND MODEL

Figure 2 shows a test rig schematic. Regulated, compressed air (coolant), throttled by a flow

control valve, flows through a sharp edge orifice flowmeter, through tubing, and through a rotating union at the bottom of a rotating shaft. The air then passes through the hollow rotating shaft and an aluminum hollow, rotating arm mounted perpendicularly onto the shaft. Finally the coolant passes through the test model and exits into the lab. The test model slips into one end of the arm and the other end serves as a counter balance. An electric motor with an adjustable frequency controller turns

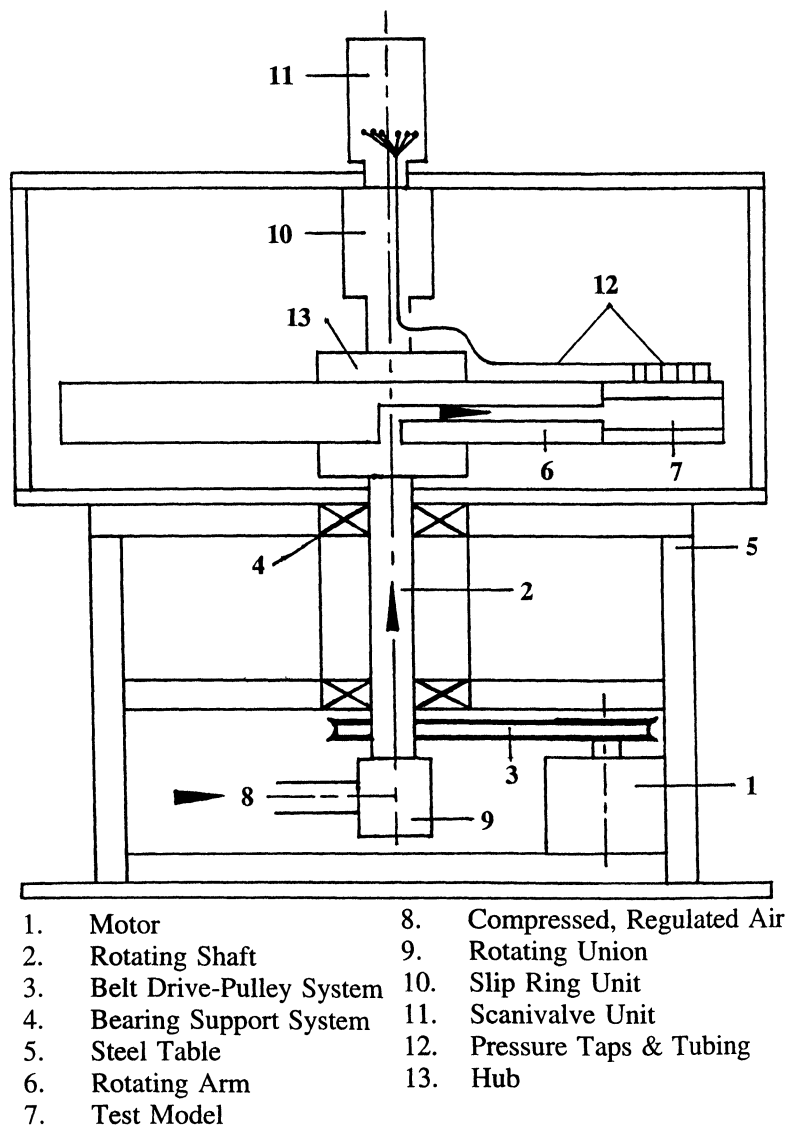


FIGURE 2 Test stand schematic.

the shaft, arm, test model, a slip ring unit and a Scanivalve unit via a toothed belt. A digital photo tachometer measures the rotating shaft speed.

Figure 1 shows top and end views of the test model. Symmetry planes exist passing through the center of the supply channel and are parallel or perpendicular to the axes of the shaft and arm. The test model consists of two mirror-imaged channels of rectangular cross section ( $2.18\text{ cm} \times 0.64\text{ cm}$ ) which flank (in and opposite to the direction of rotation) the square cross section supply channel ( $1.91\text{ cm} \times 1.91\text{ cm}$ ). The channels are at a mean rotating radius to jet diameter ratio of 397 and have a channel length to jet diameter ratio of 151. The jet diameter is 1.59 mm. Circular jet holes of length to jet diameter ratio of 5.2 are through the jet walls and connect the supply channel to each twin channel. The jet holes create jets that impinge perpendicularly on the target walls with the distance between the jet hole exit and target wall to jet diameter ratio of 4.0. The jet arrays for both twin channels are square with 30 rows in the radial direction with only two jets in each row for 60 jets per channel, 120 impinging jets in total. The distance between jet centers to jet diameter ratio is 5.0 for these square arrays. In the test model, air first enters the supply channel, flows through the 120 jet holes, impinging on the target wall in the trailing channel and on the target wall in the leading channel. From the leading (trailing) channel, spent air exits in (opposite to) the direction of rotation through 24 extraction holes in the target walls with diameter  $D_e = 2.54\text{ mm}$  (alternating holes for 50% reduction) and length-to-diameter ratio of 10.5. These extraction holes are in a single row and staggered with respect to the jet impingement arrays with  $N_e/N_j = 24/60$ ,  $A_e/A_j = 2.56$ . However, extraction hole spacing along the target walls alternates between  $X/D = 2.5$  and 5.3 (see Fig. 3, Section B-B). Finally there are four additional holes (diameter = 2.54 cm and length-to-diameter ratio = 4.9) through the end cap of the center supply channel. These four holes route part of the supply channel air to the outside of the cap bypassing the heated channels.

Figure 1 also shows that the channel walls are each made of six isolated copper plates to obtain regionally averaged heat transfer measurements. For each target wall plate, the face is  $3.81\text{ cm} \times 1.91\text{ cm}$  and the thickness is 3.2 mm. Ten jets are directly opposite each plate with jet area to full-face target wall area ratio of 0.027. Each target wall is separately heated by wire resistance heaters uniformly cemented in grooves on the backside of the wall's copper plates. The target wall copper plates are backed by Teflon of 2.5 cm. The other three walls in each of the twin channels are similar in construction, but remain unheated for tests in this paper. Thin 1.59 mm wide Teflon partitions separate and insulate the copper plates. Thermocouples (T type, Copper–Constantan with Teflon–Neoflon PFA duplex insulation) in the copper plates measure wall temperatures which are regionally averaged due to the conductivity of the copper and the pointwise distribution of surface heat transfer coefficients beneath impinging jets. Thermocouples in the center of all three channels measure local coolant temperatures. The thermocouples in the channels are at ends of wires protruding from one jet wall in the supply channel and from selected Teflon partitions of the jet walls in the heated channels (see Fig. 3). These wires remain perpendicular to the walls with coolant flow and rotation. There are no coolant temperature corrections since the jet flows are at low Mach numbers ( $< 0.3$ ). An air passage of circular cross section (2.06 cm diameter, 40.6 cm in length) immediately upstream of the center supply channel is made of Teflon for insulation. A slip ring unit mounts directly atop a hub that connects the shaft to the arm. This 100 channel slip ring unit transfers thermocouple outputs to a data logger interfaced to a personal computer and variable transformer outputs to the wire resistance heaters.

Flow distribution measurements are obtained from six wall static pressure taps in each of the three channels. A nineteenth tap is at the inlet to the supply channel. Eight additional pressure taps are mounted to the external surface of and at the leading and trailing edges of the rotating arm.

| $Re_{jet}$       | 5000   |        | 10000  |        |
|------------------|--------|--------|--------|--------|
| rpm              | 0      | 800    | 0      | 800    |
| Leading Channel  | ▲—▲    | △---△  | ◆—◆    | ◇---◇  |
| Leading Exit     | ▲····▲ | △····△ | ◆····◆ | ◇····◇ |
| Trailing Channel | ▼—▼    | ▽---▽  | ■—■    | □---□  |
| Trailing Exit    | ▼····▼ | ▽····▽ | ■····■ | □····□ |
| Center Channel   | ●---●  | ○---○  | +---+  | x---x  |

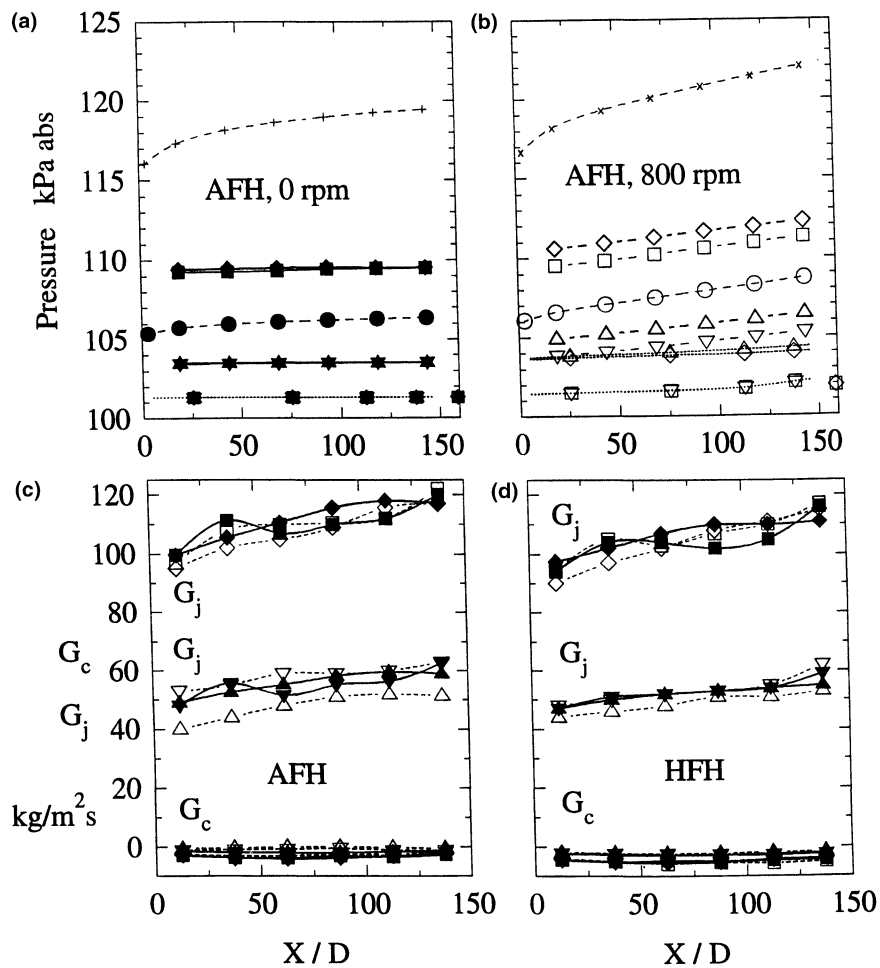


FIGURE 3 Pressure and mass flux distributions for  $Re_{jet} = 5000$  and  $10,000$  at  $\Omega = 0$  and  $800$  rpm.

Of these four taps each are for the extraction hole exits of the leading and trailing channels. Tubes from the taps are routed through the center of and connected to a Scanivalve unit mounted atop the

slip ring unit. The Scanivalve unit rotates with the arm, shaft, and slip ring unit and contains a multipoint fluid switch, a stepper motor, a differential type pressure transducer, and an encoder.

The multiport fluid switch connects only one pressure tap-port combination at a time to the transducer for pressure measurement. The motor moves the switch to different ports and the encoder indicates the selected tap-port. One additional port is connected to a u-tube manometer for transducer calibration. The Scanivalve motor control, input to and output from the pressure transducer, and output of the encoder are also via slip ring channels.

### TEST PROCEDURE AND DATA REDUCTION

The flow distribution tests are conducted adiabatically. This investigation assumes the mass flow distribution throughout the test model is relatively unchanged by heat addition during heat transfer tests. For flow tests, the rotating speed is set and then the throttle valve is adjusted for a desired total flow rate. An inclined manometer measures pressure drops across the sharp edge orifice flowmeter for total flow rate calculations. Finally, static pressure readings are recorded at all tap locations using the Scanivalve unit. Pre- and post-test pressure transducer calibrations are performed. For non-rotating flow tests, the leading and trailing channel exit pressures at the end cap holes are at atmospheric lab conditions. By interpolating for inlet and exit jet hole pressures among the measured pressures, the hole pressure drops, the air jet velocities, the discharge coefficients and thus the flow rate ratio in each of the 120 jets, the 48 extraction hole, and the four holes in the end cap are calculated. Non-rotating discharge coefficients are calculated using the overall mass balance for the test model and are locally adjusted for the pressure differences/jet Reynolds numbers for each jet. The calculations assume one-dimensional flow and use ideal gas equation of state, continuity, and adiabatic compressible flow relations. Since the variation of hole discharge coefficient with local impingement jet Reynolds number is known from non-rotating results, this variation is used to estimate discharge coefficients for rotating conditions.

If a discrepancy occurs for overall mass balance for rotating tests, the local discharge coefficients are adjusted in proportion to the amount of flow through each jet hole. This preserves the slight increase of discharge coefficient with increasing  $Re_{jet}$ .

For heat transfer results, regional convective heat transfer coefficient  $h$  is

$$h = (q_{total} - q_{loss}) / [(A_{tw} + N_e(A_{eh} - A_e))(T_w - T_c)], \quad (1)$$

where  $q_{total}$  is the heat generated in a copper plate for heat transfer tests;  $q_{loss}$  is the heat loss for a plate;  $A_{tw} + N_e(A_{eh} - A_e)$  is the net wetted or exposed target plate surface area (full-face area – total extraction hole area [ $N_e\pi D_c^2/4$ ] + total extraction hole sides area [ $N_e\pi D_e \times$  plate thickness]);  $T_w$  is a plate temperature; and  $T_c$  is a temperature for the coolant adjacent to the center of the heated plates which is obtained by spatial interpolation between measured local air temperatures. For heat transfer tests, the rotating speed and overall coolant flow rate are set and the transformers adjusted until the desired heated wall temperatures are reached. The plate and coolant temperatures, the voltages and currents for each heater, and the overall flow rate are recorded at steady state conditions. The  $q_{total}$  (per plate) = (voltage  $\times$  current)  $\times$  (length of heating wire cemented in each plate/total length of heating wire). The variance in length of wire cemented to a plate is less than 0.5% of the total wire length for a wall. This provides a nearly uniform wall heat flux boundary condition. The heat loss per plate ( $q_{loss}$ ) is the amount of heat conducted and radiated into the test model and test stand but not convected directly to the coolant. Tests for heat loss are performed at the same rotating speed, with no coolant flow, and with the extraction and end cap holes covered with tape to prevent forced convection induced by rotation. Several input power levels are used to determine heat losses for all plates as functions of their corresponding temperature differences between each plate and surroundings (room conditions).

The uncertainty of the local heat transfer depends on the net heat input ( $q_{\text{total}} - q_{\text{loss}}$ ) to the coolant and the local wall-to-coolant temperature difference. This uncertainty increases with decreasing temperature difference and decreasing net heat input. Considering the method by Kline and McClintock (1953), the typical uncertainty in the Nusselt number is estimated less than 8% for  $Re_{\text{jet}} = 10,000$ . However, the maximum uncertainty could be up to 12% for  $Re_{\text{jet}} = 5000$ , at the largest radial location ( $X/D = 138$ ). The heat conduction between a plate and its neighbors is estimated to be less than 1% of the net heat input for each of the plates at  $Re_{\text{jet}} = 5000$ . However, this percentage decreases to 0.5% at  $Re_{\text{jet}} = 10,000$ . For  $Re_{\text{jet}} = 5000$ , as the rotation rate increases from 0 to 800 rpm, the average ratio of the heat loss power to the total plate power increases from 0.09 to 0.16 for the target walls. At  $Re_{\text{jet}} = 10,000$ , the average ratio increases from 0.06 to 0.10 as rotation increases. The uncertainties in calculations of jet mass fluxes are about 2.5%.

## EXPERIMENTAL RESULTS AND DISCUSSION

The Nusselt number distributions for jet impingement in rotating channels for this test model geometry depends on: (1) the ratio of the test model's mean radius-to-jet-diameter, (2) the ratio of local radial distance to jet diameter, (3) the average jet Reynolds number, (4) the Prandtl number, (5) the jet rotation number, (6) the wall-to-coolant temperature difference, (7) the jet flow direction with respect to rotation direction, (8) the channel geometry (cross section and orientation), and (9) the exit flow configuration. The functional relationship is expressed as

$$Nu = f(r_m/D, X/D, Re_{\text{jet}}, Pr, Ro, (T_w - T_c)/T_w, \text{jet direction, channel geometry, exit flow configuration}), \quad (2)$$

where  $Pr = 0.72$  and  $r_m/D = 397$ . Operating conditions are:  $Re_{\text{jet}} = 5000$  and  $10,000$ , and  $\Omega = 0, 400,$

and 800 rpm, combining to produce  $Ro = 0.0, 0.0008, 0.0015,$  and  $0.0028$ . For the target walls, the wall-to-coolant temperature difference ratio is 0.0855 for 0 rpm, 0.0855 for 400 rpm, and 0.0855 and 0.129 for 800 rpm, combining to produce  $Gr \sim 10^4$ . It is noted that typical values of  $Re_{\text{jet}}, Ro,$  and  $Gr$  in engine representative conditions are about 8000, 0.005, and  $10^5$ , respectively. For the two exit configurations, tests with 100% of the extraction holes open are denoted AFH, while tests with 50% of the extraction holes open are denoted HFH. For HFH, every other extraction hole is plugged starting with a plugged hole at the outer most radius. For comparisons, tests with the cross flow exit configuration are denoted XF (Parsons and Han, 1998). The other three walls in each of the twin channels are insulated and unheated. Air properties are at the average of the measured inlet and exit coolant temperatures.

### Flow Distribution

For low speed flows in non-rotating geometries, local velocity changes depend on the pressure differences or gradients. Figure 3(a) and (b) shows channel static and extraction hole exit pressures versus channel location for AFH at 0 and 800 rpm, respectively. For these figures, a set of five curves for each jet Reynolds number shows the center supply channel, leading channel, trailing channel, leading exit, and trailing exit pressures. However, Fig. 3(c) shows calculated mass fluxes  $G_j (= \rho_j V_j)$  for the jet flow direction and  $G_c (= \rho_c V_c)$  for the channel cross flow direction for AFH while Fig. 3(d) shows these results for HFH. In Fig. 3(c) and (d), results for 0 and 800 rpm are presented.

### Non-Rotating Results

By observation, the trend of relative pressure differences among a set of curves is the same regardless of Reynolds number. For non-rotation, the leading and trailing channel pressure curves are constant with respect to channel location indicating no significant cross flow velocity ( $G_c \approx 0$ ) along the length

of these channels. Since leading and trailing channel pressures are the same for a fixed Reynolds number, supply-to-leading pressure differences and supply-to-trailing pressure difference are also the same. Thus for each jet hole location ( $X/D$ ) the jet velocities and the local jet mass fluxes are the same from the supply channel toward the leading channel target wall and toward the trailing channel target wall. Jet velocities and local jet mass fluxes increase slightly as  $X/D$  increases. Similarly the leading channel-to-leading exit and trailing channel-to-trailing exit pressure differences are the same too. Thus for each extraction hole location the velocities of extraction hole flows are the same. Therefore for the non-rotating test model, the flow distribution is symmetric with respect to the supply channel centerline. Also the supply channel, impingement jet and extraction hole flows, and local jet mass fluxes decrease as  $Re_{jet}$  decreases. Mass flow calculations indicate non-rotating impingement jet discharge coefficients increase slightly as expected from 0.68 to 0.72 as local  $Re_{jet}$  increases from 4000 to 13,000, respectively. Discharge coefficients for the extraction holes also increase from 0.76 to 0.90 as  $Re_{ch}$  increases from 9000 to 30,000 as expected for extraction holes with a large length-to-diameter ratio.

In comparing AFH (Fig. 3(a)) with HFH (data not presented) the supply-to-channel pressure differences for both configurations are the same. However due to the reduced number of extraction holes for HFH, only the channel-to-exit pressure differences for HFH are higher than those AFH. Thus for HFH, only the extraction hole and near extraction hole target wall surface velocities are higher than those for AFH. The identical natures of Fig. 3(c) and (d) confirm this for AFH and HFH.

### Rotating Results

Flow distribution results for rotating tests are slightly more complex than those for stationary tests. First, as shown in Fig. 4, rotation produces centrifugal forces (radially outward), Coriolis

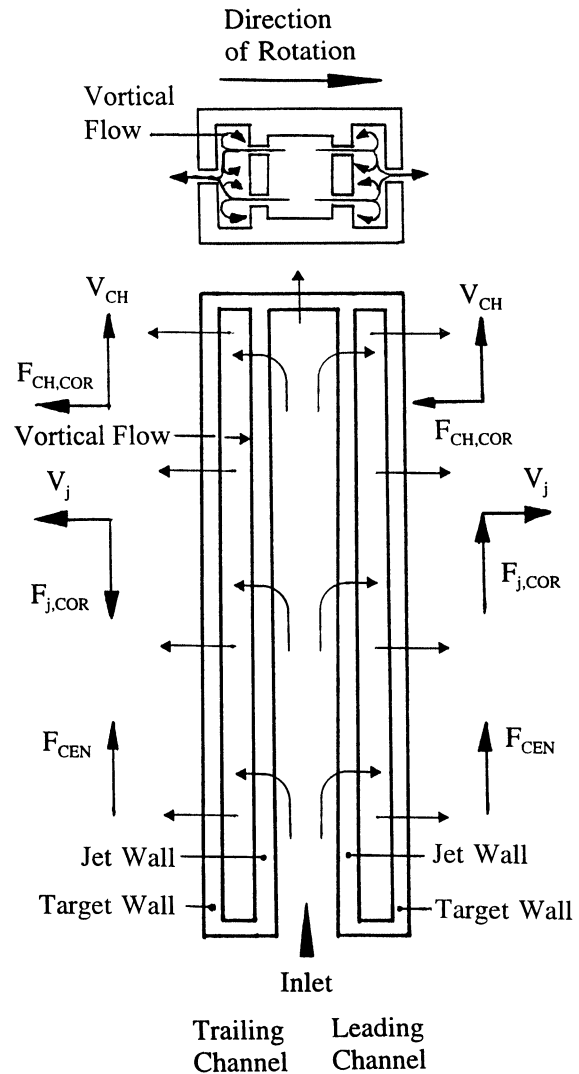


FIGURE 4 Schematic including velocities and forces.

forces (in various directions) and buoyancy forces (that depend on local air density/temperature variations) that create secondary flows and alter air flow in the test model. Second, as for solid body rotation, pressure in the radial ( $r$  or  $X$ ) direction increases with radius due to the pressure force opposing the fluid centrifugal force. Third, the channel walls act like radial vanes on a pump and try to transfer energy (in the form of pressure and/or velocity) to the air. However, pumping in a channel for this test model geometry occurs only

if the product of local channel rotating velocity and the absolute air velocity in the rotating direction changes as a fluid particle moves from one location to another. Thus without radial fluid motion (channel cross flow) this product does not change and little or no pumping occurs. Finally, the arm rotation creates complicated flow and pressure fields around the outside of the arm and the end cap. Figure 4 also shows qualitative flow schematics for the test model.

Figure 3(b) shows pressure distributions for rotating AFH tests and Fig. 3(c) and (d) also shows local mass flux distributions under rotating conditions for AFH and HFH, respectively. Comparing Fig. 3(a) and (b) shows one effect of rotation. This is the pressure difference from the inner radius ( $X/D=19$ ) to the outer radius ( $X/D=144$ ) for any channel and Reynolds number with rotation is approximately 1.5 kPa greater than their corresponding pressure differences without rotation. This is due to the effect of the air centrifugal force. Another effect of rotation is the change of extraction hole exit pressures. Recall taps for these pressures are at the leading edge (for the leading channel exit) and trailing edge (for the trailing channel exit) of the rotating arm. Since the arm leading edge becomes a stagnation point, static (also total) pressures are greater than ambient conditions (see Fig. 3(b)). These pressures increase with radius as dynamic pressure increases with local rotating arm speed. The trailing edge is at a stagnation point in the wake region behind the arm, which is rotating in free air. Thus these pressures are nearly atmospheric.

Further comparisons between Fig. 3(a) and (b) show that the pressure distributions have the same trends for rotation as for non-rotation. For a fixed jet Reynolds number, the supply channel pressure is highest and the leading and trailing channel pressures are higher than their respective exit pressures. Since rotation increases the leading exit pressures the leading channel pressures respond and are higher than the trailing channel pressures. Thus jet impingement velocities and local jet mass fluxes for the trailing channel target wall with

rotation are equal to or slightly greater than those for both target walls without rotation which are in turn slightly greater than those for the leading channel target wall with rotation. Correspondingly with rotation, the trailing channel, target wall extraction hole velocities are slightly greater than those for the leading channel.

## Heat Transfer

### Non-Rotating Results

Figure 5(a) shows non-rotating Nusselt numbers  $Nu_{0,AFH}$  and  $Nu_{0,HFH}$  versus channel location ( $X/D$ ) for the Reynolds numbers at  $(T_w - T_j)/T_w = 0.0855$ . For each jet Reynolds number, the

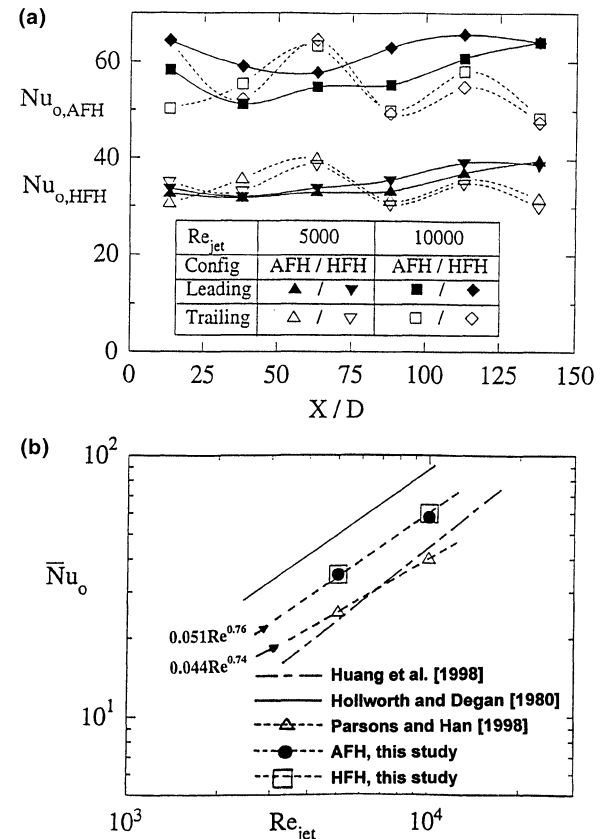


FIGURE 5 Non-rotating results: (a) – non-rotating Nusselt number versus channel location for target wall at  $(T_w - T_j)/T_w = 0.0855$ ; (b) – Wall average Nusselt number versus  $Re_{jet}$  for present data and comparison with other investigations.

non-rotating Nusselt numbers are approximately constant with channel location, equal for corresponding AFH and HFH results, and equal on average between corresponding leading and trailing channels. This confirms that the non-rotating test model operates symmetrically for flow and heat transfer. And as  $Re_{jet}$  increases so do non-rotating Nusselt numbers. This is because as impingement jet flow and wall surface flow increases, the wall boundary layers thin and heat transfer increases. Also it appears the increases in target wall surface and extraction hole velocities for HFH as compared to those for AFH compensate for the reduction in the number of extraction holes.

To show the integrity of the experimental method and test model, bulk mean temperature rise calculated from an energy balance is within 10% and 30% of the measured local air temperature rise for  $Re_{jet} = 5000$  and 10,000, respectively. Figure 5(b) shows the 12-plate average of non-rotating Nusselt numbers (plotted as  $\bar{Nu}_0$ ) versus  $Re_{jet}$  and comparisons with other jet impingement/extraction and cross flow exit heat transfer results for non-rotating conditions.

Huang *et al.* (1998), and Parsons and Han (1998) used the similar jet spacing and jet impinging distance. In both studies jets impinged on the target wall and the spent air exited at one end of the impingement channel (without film extraction holes on the target wall) which creates a cross flow effect on other jets and reduces the impingement cooling effect on the target wall. They both produce about the same level of Nusselt numbers over the range of  $Re_{jet}$ . This study used the identical jet spacing and jet impinging distance as those in Parsons and Han (1998) except the target wall with film extraction holes. The present AFH and HFH results are closer to each other but higher than those of Parsons and Han (1998). This may be because the film extraction holes create a boundary-layer suction, which thins the boundary layers, and produces high local heat transfer coefficients in the vicinities of the film extraction holes. However, the present results are lower than those in Hollworth and Dagan (1980). This may be because

they use a different film extraction hole diameter and its distribution, although they use a similar jet spacing and jet impinging distance. The area ratio of film extraction hole to impinging jet hole ( $A_e/A_j$ ) is 2.567 in this study while this ratio is 1 in Hollworth and Dagan (1980). It seems that the smaller  $A_e/A_j$  ratio is more effective to produce high impinging heat transfer from the target wall with film extraction holes.

### Rotating Results

#### *Effect of Rotation Relative to Non-Rotation*

Figure 6(a) and (b) shows the effect of rotation on the local Nusselt number ratio ( $Nu_{AFH}/Nu_{0,AFH}$ ). Note that the Nusselt number ratio is the local Nusselt number divided by the corresponding measured local Nusselt number for non-rotation (see Fig. 5(a)). Figure 6(a) shows results at  $Re_{jet} = 5000$  for a set of higher rotation numbers  $Ro = 0.0, 0.0015, \text{ and } 0.0028$  ( $\Omega = 0, 400, \text{ and } 800$  rpm, respectively) while Fig. 6(b) shows results at  $Re_{jet} = 10,000$  for a set of lower rotation numbers  $Ro = 0.0, 0.0008, \text{ and } 0.0015$  ( $\Omega = 0, 400, \text{ and } 800$  rpm, respectively). Non-dimensional parameter  $Ro$  relates rotation effects and can be expressed as: (centrifugal force/jet Coriolis force)  $\times (D/\text{local radius from axis of rotation})$ . Figure 6(a) shows the target wall Nusselt number ratios decrease by up to 25% as compared to the non-rotating value of 1.0. For the leading channel, the jet, target wall surface and extraction hole velocities are reduced as compared to results for non-rotating target walls and for trailing channel walls under rotation. In addition, the centrifugal force combines with the Coriolis force to bend the jets away from the leading channel target wall. These thicken the boundary layers and decrease the heat transfer coefficients. For the trailing channel, the jet, target wall surface, and extraction hole velocities may increase as compared to non-rotating results, but the centrifugal force deflects the jet from impinging on the target wall. Thus the net effect in the decreases in Nusselt number ratio are less for the trailing channel than those decreases for the

| $Re_{jet}$ |   | 10000  | 10000          | 5000   | 5000           |
|------------|---|--------|----------------|--------|----------------|
| rpm        | 0 | 400    | 800            | 400    | 800            |
| Ro         | 0 | 0.0008 | 0.0015         | 0.0015 | 0.0028         |
| Leading    | — | ◆      | AFH ▲<br>HFH ▼ | ●      | AFH ■<br>HFH + |
| Trailing   | — | ◇      | AFH △<br>HFH ▽ | ○      | AFH □<br>HFH × |

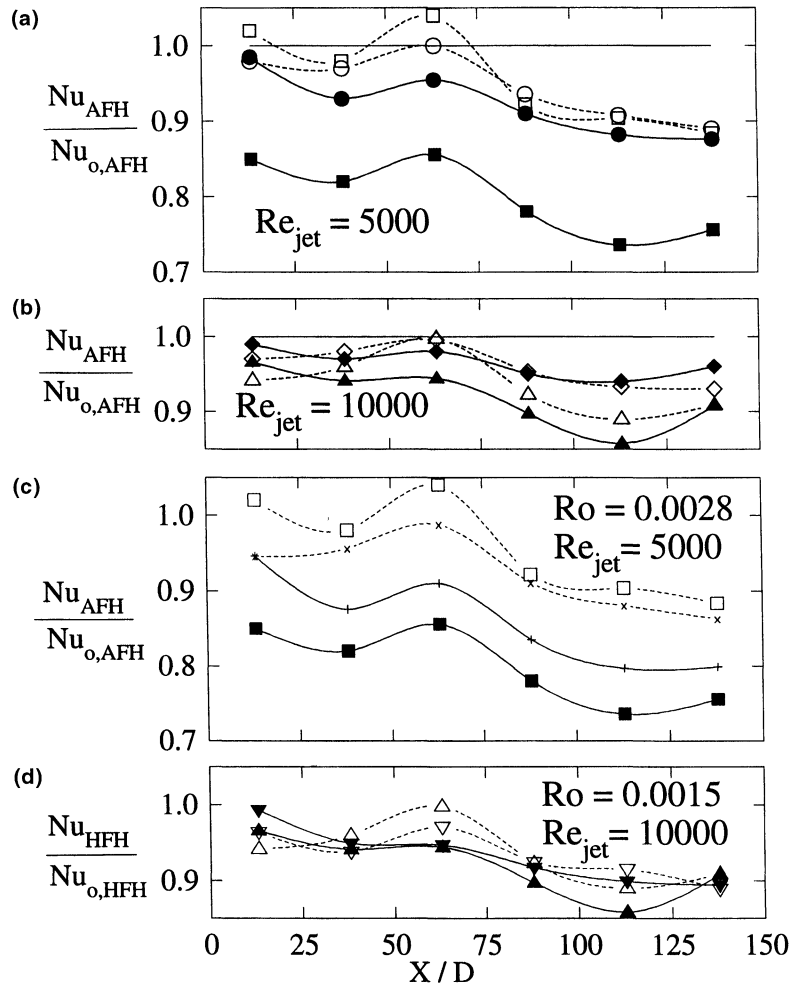


FIGURE 6 Effect of rotation on target wall Nusselt number ratio at  $(T_w - T_j)/T_w = 0.0855$ : (a) –  $Re_{jet} = 5000$ ; (b) –  $Re_{jet} = 10,000$ ; (c) –  $Ro = 0.0028$  for AFH and HFH; (d) –  $Ro = 0.0015$  for AFH and HFH.

leading channel. These decreases are greater for  $X/D > 75$  where there are greater jet bending Coriolis and centrifugal forces than the decreases for  $X/D < 75$ .

Figure 6(b) for  $Re_{jet} = 10,000$  shows Nusselt number ratios for the target walls are between 1.0 and 0.85. Also at constant  $Re_{jet} = 10,000$ , as  $Ro$  increases the differences between the Nusselt number

ratios for both target walls and 1.0 increase. However, these differences for lower rotation numbers (Fig. 6(b)) are reduced as compared to those differences at  $Re_{jet} = 5000$  for higher rotation numbers (Fig. 6(a)). Therefore the effect of rotation (to reduce Nusselt number ratio) increases as  $Ro$  increases.

#### Effect of Exit Flow Configuration

Figure 6(c) and (d) show Nusselt number ratios for AFH and HFH at  $Ro = 0.0028$ ,  $Re_{jet} = 5000$ , and  $Ro = 0.0015$ ,  $Re_{jet} = 10,000$ , respectively. The rotation effect for AFH (explained for Fig. 6(a) above) decreases as the number of extraction holes is reduced. The pressure drop across the leading and trailing extraction holes for HFH is increased, with respect to that for AFH. Therefore, the changes for the holes exit pressures caused by rotation are relatively smaller for HFH and thus so are the changes for flow and heat transfer. This caused the reduced differences between leading and trailing target wall Nusselt number ratios as compared to those differences for AFH. However, other effects (i.e., the Coriolis and centrifugal forces bending jets from target walls) decrease the Nusselt number ratio as  $X/D$  increases. In Fig. 6(c) these differences are larger at  $Ro = 0.0028$  than those in Fig. 6(d) at  $Ro = 0.0015$ .

#### Effect of Reynolds Number

Figure 7 shows the effect of Reynolds number on Nusselt number ratio while holding  $Ro$  at 0.0015 for AFH. The rotation number is held constant by

varying the rotation speed  $\Omega$  and  $\bar{V}_j$  (or  $Re_{jet}$ ): i.e.  $\Omega = 400$  rpm,  $Re_{jet} = 5000$ , and  $\Omega = 800$  rpm,  $Re_{jet} = 10,000$ . The results show Nusselt number ratios are within 2% as either Reynolds number or rotation speed changes at constant rotation number for corresponding walls and channel locations. Thus it appears that the rotation number is a characteristic non-dimensional parameter for rotating jet impingement regardless of the exit flow configuration (cross flow – Parsons and Han (1998) and target wall extraction – present results).

#### Effect of Wall-to-Coolant Temperature Difference Ratio

Figure 8 shows the effect of the target wall-to-coolant temperature difference ratio  $((T_w - T_j)/T_w)$  on Nusselt number ratio for  $Re_{jet} = 5000$ ,  $Ro = 0.0028$ . In Fig. 8, the target wall Nusselt number ratios for the leading and trailing channels vary within 25% below 1.0. The main reason is the effect of rotation described above. However, as  $(T_w - T_j)/T_w$  increases, the Nusselt number ratio varies up to 2% only while other parameters are held constant. The jet, vortical, and secondary flows and their corresponding Coriolis forces are in many directions and thoroughly mix the air in the channels. This produces small local variations of temperature and density. Recall that the buoyancy body force  $(\Delta\rho_{local}(\Omega^2 r + \Omega V_{local}))$  depends on local density variation. Thus as wall-to-coolant temperature difference ratio and thus local temperature and density variation increase, the effects of buoyancy forces remain small and are in the same directions as

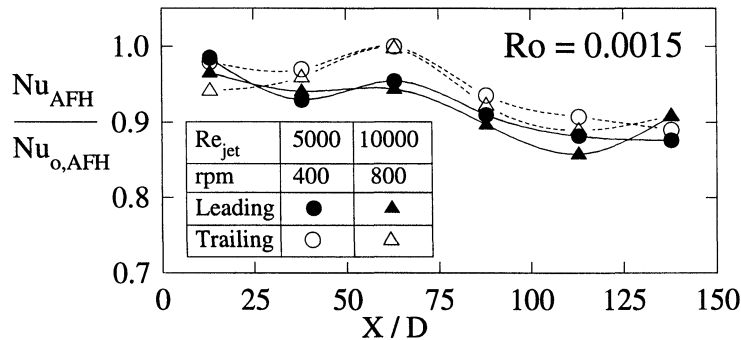


FIGURE 7 Effect of Reynolds number on target wall Nusselt number ratio.

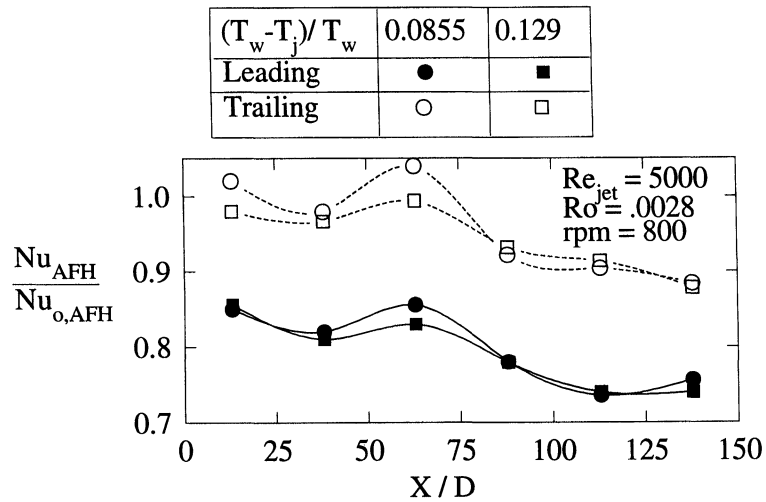


FIGURE 8 Effect of wall-to-coolant temperature difference ratio on target wall Nusselt number ratio.

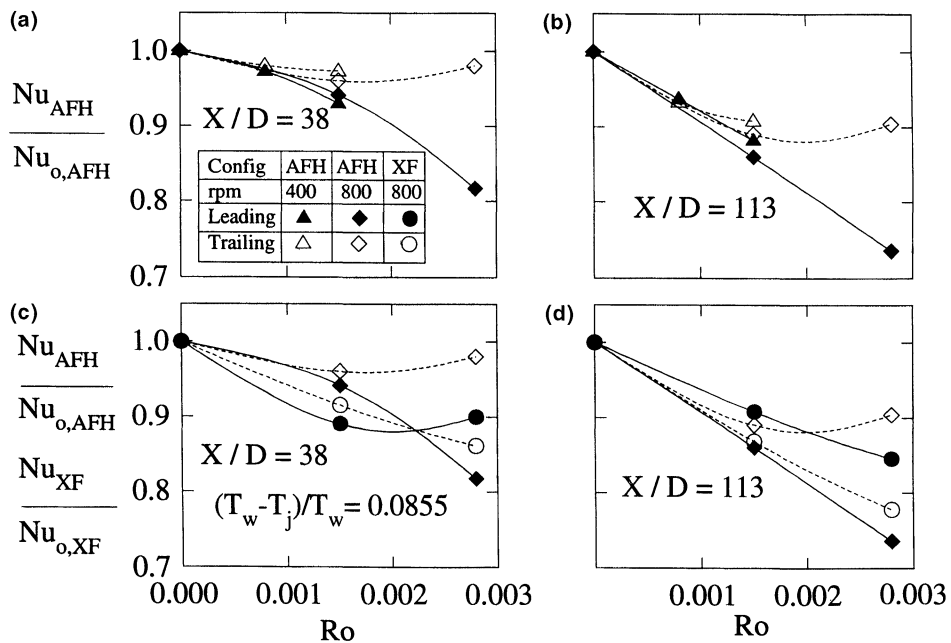


FIGURE 9 Effect of rotation number on target wall Nusselt number ratio: (a) -  $X/D=38$ , AFH; (b) -  $X/D=113$ , AFH; (c) -  $X/D=38$ , AFH and XF; (d) -  $X/D=113$ , AFH and XF.

those for local Coriolis and centrifugal forces. It is noted that this may be true at low rotational speeds of the present test conditions ( $Gr \sim 10^4$ ) but it is unlikely to be true at high rotational speeds of real engine conditions ( $Gr \sim 10^5$ ) where rotational buoyancy effects may be significant.

*Effects of Rotation Number at Selected Channel Locations*

Figure 9(a) and (b) shows the effect of rotation number on Nusselt number ratio at channel locations  $X/D=38$  and  $113$ , respectively, at  $(T_w - T_j)/T_w=0.0855$  and for AFH. First, these

figures show that at constant  $Ro$  the Nusselt number ratios are the same for AFH at 400 rpm as for 800 rpm ( $Ro$  is a key correlating parameter). Second, Fig. 9(a) for  $X/D=38$  shows that as  $Ro$  increases, these ratios for both target walls decrease by up to 20% while Fig. 9(b) for  $X/D=113$  shows that these ratios decrease up to 25%. Third, the decreases in these ratios for the leading channel are greater than those for the trailing channel for AFH. Figure 9(c) and (d) shows Nusselt number ratios also at  $X/D=38$  and 113, respectively, but for AFH and XF exit configurations. Conversely, the decreases in these ratios for the trailing channel are generally greater than those for the leading channel for XF. Finally as rotation number increases, the differences between these ratios for the leading and trailing channel target walls increase more for AFH than those differences for XF.

## CONCLUSIONS

The main conclusions are as follows:

- (1) For a square array of jets impinging normally on one wall in a rectangular channel with coolant extraction through the target walls as the exit condition, jet flow velocities increase slightly as  $X/D$  increases. For a given jet Reynolds number, the pressure and thus flow distributions for rotation differ slightly from those without rotation. Under rotation, jet flows toward the leading channel target wall are reduced as compared to jet flows toward the trailing channel target wall.
- (2) At constant jet Reynolds number and non-rotating conditions, as  $X/D$  increases, the leading and trailing target wall Nusselt numbers are nearly equal and constant. Nusselt numbers increase with jet Reynolds number. This trend is the same as for other researchers. However, the Nusselt numbers on target walls with film extraction holes are higher than those without film extraction holes (i.e., with cross flow effect).

- (3) As the rotation number increases up to 0.0028, the target wall Nusselt number ratios for the leading (jet flow in the direction of rotation) and trailing (jet flow opposite to the direction of rotation) channels decrease below the non-rotating value up to 25% and 20%, respectively.
- (4) As wall-to-coolant temperature difference ratio  $(T_w - T_j)/T_w$  increases from 0.0855 to 0.129 under low rotational speed conditions ( $Gr \sim 10^4$ ), the target wall Nusselt number ratios only vary up to 2%. However, the rotational buoyancy effects may be significant under high-speed engine conditions ( $Gr \sim 10^5$ ).
- (5) For parameter ranges in this paper, varying the jet Reynolds number while holding other parameters constant ( $Ro$  constant) had a small effect on target wall Nusselt number ratios for both channels.
- (6) With other parameters constant, the effect of rotation on Nusselt number ratios for AFH is greater than on these ratios for HFH. The effect of rotation (to decrease Nusselt number ratio) is greater for leading channel target walls of AFH/HFH configurations than for trailing channel target walls. For the cross flow exit condition, the reverse is true.

## NOMENCLATURE

|          |  |
|----------|--|
| $A$      | area   |
| $D, D_j$ | impingement jet hole diameter –<br>1.59 mm (0.0625 inch)                   |
| $D_e$    | extraction hole diameter –<br>2.54 mm (0.100 inch)                         |
| $F$      | fluid body forces due to rotation  |
| $G$      | mass flux based on cross sectional<br>area of flow                         |
| $Gr$     | average jet Grashof number<br>$[(Ro)^2(Re_{jet})^2(r_m/D)(T_w - T_j)/T_w]$ |
| $h$      | heat transfer coefficient  |
| $k$      | thermal conductivity of coolant<br>(air)                                   |
| $N$      | number of jet holes  |

|                    |  |    |                 |
|--------------------|--|----|-----------------|
| $Nu$               | Nusselt number ( $hD/k$ ) for rotating conditions  | j  | jet             |
| $Nu_0$             | non-rotating Nusselt number at corresponding location  | tw | target wall     |
| $q_{\text{loss}}$  | heat transfer rate from heated wall to test model  | w  | wall (or plate) |
| $q_{\text{total}}$ | total heat transfer rate from heated wall  | XF | cross flow      |
| $Re_{\text{jet}}$  | average jet hole Reynolds number ( $\rho_j \bar{V}_j D / \mu$ )                              |    |                 |
| $Ro$               | average jet rotation number ( $\Omega D / \bar{V}_j$ )                                       |    |                 |
| $r_m$              | radial distance from axis of rotation to test model's mean radius                            |    |                 |
| $T_c$              | measured (and interpolated) coolant temperature in channels                                  |    |                 |
| $T_j$              | inlet or jet temperature, $\approx 21-27^\circ\text{C}$                                      |    |                 |
| $T_w$              | wall (plate) temperature   |    |                 |
| $V$                | local velocity   |    |                 |
| $\bar{V}$          | average velocity   |    |                 |
| $X$                | radially outward distance from test model inlet (see Fig. 1)                                 |    |                 |
| $(T_w - T_j)/T_w$  | wall-to-coolant temperature difference normalized by absolute wall temperature [ $R^\circ$ ] |    |                 |

### Greek Symbols

|          |  |
|----------|--|
| $\mu$    | air dynamic viscosity                                      |
| $\rho$   | coolant density  |
| $\Omega$ | rotational speed; rad/s in $Ro$ and forces, rpm in figures |

### Subscripts

|     |   |
|-----|---|
| AFH | All Film Hole case (100% extraction hole tests) |
| CH  | channel   |
| COR | due to Coriolis force                           |
| CEN | due to centrifugal force                        |
| e   | extraction                                      |
| eh  | extraction hole                                 |
| HFH | Half Film Hole case (50% extraction hole tests) |

### Acknowledgments

This investigation was supported by the Texas Higher Education Coordinating Board – Advanced Technology program under grant number 999903-165. This project was also partially supported by GE-Aircraft Engines. Their support is greatly appreciated.

### References

- Al Dabagh, A.M., Andrews, G.E., Abdul Hussain, R.A.A., Hussain, C.I., Nazari, A. and Wu, J. (1990) Impingement/effusion cooling: the influence of the number of impingement holes and pressure loss on the heat transfer coefficient, *ASME Journal of Turbomachinery*, **112**, 467–476.
- Andrews, G.E., Asere, A.A., Hussain, C.I., Mkpadi, M.C. and Nazari, A. (1988) Impingement/effusion cooling: Overall wall heat transfer, *ASME Paper No. 88-GT-290*.
- Bunker, R.S. and Metzger, D.E. (1990) Local heat transfer in internally cooled turbine airfoil leading edge regions: Part I – Impingement cooling without film coolant extraction, *ASME Journal of Turbomachinery*, **112**, 451–458.
- Chance, J.L. (1974) Experimental investigation of air impingement heat transfer under an array of round jets, *TAPPI*, **57**, 108–112.
- Epstein, A.H., Kerrebrock, J.L., Koo, J.J. and Preiser, U.Z. (1985) Rotational effects on impingement cooling, *Symposium on Transport Phenomena in Rotating Machinery*, April 28–May 3, Honolulu, Hawaii.
- Florschuetz, L.W., Truman, C.R. and Metzger, D.E. (1981) Streamwise flow and heat transfer distributions for jet array impingement with cross flow, *ASME Journal of Heat Transfer*, **103**, 337–342.
- Hollworth, B.R. and Dagan, L. (1980) Arrays of impinging jets with spent fluid removal through vent holes on the target surface, Part 1: Average heat transfer, *ASME Journal of Engineering for Power*, **102**, 994–999.
- Hollworth, B.R., Lehmann, G. and Rosiczkowski, J. (1983) Arrays of impinging jets with spent fluid removal through vent holes on the target surface, Part 2: Local heat transfer, *ASME Journal of Engineering for Power*, **105**, 393–402.
- Huang, Y., Ekkad, S. and Han, J.C. (1998) Detailed heat transfer distribution under an array of orthogonally impinging jets, *AIAA Journal of Thermophysics and Heat Transfer*, **12**, 73–79.
- Kercher, D.M. and Tabakoff, W. (1970) Heat transfer by a square array of round air jets impinging perpendicular to a flat surface including the effect of spent air, *ASME Journal of Engineering for Power*, **92**, 73–82.
- Kline, S.J. and McClintock, F.A. (1953) Describing uncertainties in single-sample experiments, *Mechanical Engineering*, **75**, 3–8.
- Mattern, Ch. and Hennecke, D.K. (1996) The influence of rotation on impingement cooling, *TurboExpo*, Birmingham, United Kingdom, *ASME Paper No. 96-GT-161*.

- Metzger, D.E. and Bunker, R.S. (1990) Local heat transfer in internally cooled turbine airfoil leading edge regions: Part II – impingement cooling with film coolant extraction, *ASME Journal of Turbomachinery*, **112**, 459–466.
- Parsons, J.A. and Han, J.C. (1998) Rotation effect on jet impingement heat transfer in smooth rectangular channels with heated target walls and radially outward cross flow, *International Journal of Heat and Mass Transfer*, **41**, 2059–2071.
- Parsons, J.A., Han, J.C. and Lee, C.P. (1998) Rotation effect on jet impingement heat transfer in smooth rectangular channels with four heated walls and radially outward cross flow, *ASME Journal of Turbomachinery*, **120**, 78–85.
- Van Treuren, K.W., Wang, Z., Ireland, P.T. and Jones, T.V. (1994) Detailed measurements of local heat transfer coefficient and adiabatic wall temperature beneath an array of impinging jets, *ASME Journal of Turbomachinery*, **116**, 369–374.



**Hindawi**

Submit your manuscripts at  
<http://www.hindawi.com>

